Design of a high-modulation-depth, low-energy silicon modulator based on coupling tuning in a resonance-split microring

Tao Wang, Mu Xu, Fei Li, Jiayang Wu, Linjie Zhou, and Yikai Su*

State Key Laboratory of Advanced Optical Communication System and Networks, Shanghai Jiao Tong University, Shanghai 200240, China
Corresponding author: yikaisu@sjtu.edu.cn

We design a silicon microring modulator based on mutual-mode coupling tuning by introducing an electrically tunable grating in the microring. By tuning the grating reflectivity that changes the mutual coupling strength, optical modulation is realized since transmission switches from a peak to a dip at the resonant wavelength with resonance-splitting in the ring. High modulation depth and low energy consumption can be achieved as sufficient grating reflectivity change can be obtained with low drive voltage. Simulations show that the proposed modulator can achieve a modulation depth of ~13 dB at 1550 nm wavelength with energy consumption of 122.3 fJ/bit.   © 2012 Optical Society of America
OCIS codes: 230.3120, 250.7360, 250.5300.

1. INTRODUCTION

Silicon electro-optic (E-O) modulators may become critical components for enabling optical interconnects on microelectronic chips [1,2]. Silicon Mach-Zehnder E-O modulators have recently been proposed and demonstrated with high performances [3–6]. These devices rely on relatively weak free carrier dispersion (FCD) effect in silicon [7,8] and therefore are typically long and require high driving power to obtain a significant modulation depth. Recently, silicon microresonators have already shown their feasibility in E-O modulators with advantages of compactness, high-speed, and low-energy-consumption [9–13]. A typical silicon microresonator based modulator consists of a microring or a microdisk with an intracavity modulation section coupled to a single bus waveguide. Based on the FCD effect, the intensity and the phase of the input light are modulated by shifting the resonance of the microcavity. However, the resonance-shift based scheme has some drawbacks. First, the modulation insertion loss increases with the reduction of drive voltage because the microcavity resonance cannot be sufficiently detuned from the input wavelength [14], implying that high drive voltage may be required. Second, the modulation cannot be chirp-free since phase variation always accompanies [15,16]. Third, the modulator has to be operated close to the critical coupling point to achieve a high extinction ratio, hence making the device very sensitive to fabrication deviations [17]. To circumvent the drawbacks of the resonance-shift based scheme, coupling-tuning based silicon ring modulators were proposed [18–21] and demonstrated [22]. However, a long Mach–Zehnder interferometer (MZI) arm of hundreds of micrometers is needed to achieve sufficient modulation depth with a moderate drive voltage, which prevents further scaling down of the device size.

Recently, optical switching was proposed [23] and experimentally demonstrated [24] based on coupled ring resonators with Vernier effect, which has been investigated on different material platforms, including SOI [25–27], polymer [28], and III-V compound semiconductors [29,30]. Furthermore, mutual mode coupling in single-ring resonators was explored [31] and utilized for many applications, such as fast light in an overcoupled region [32], continuously tunable slow- to fast-light in double-waveguide coupled resonators [33], dense wavelength conversion and multicasting [34], and optical up-conversion in radio-over-fiber systems [35]. Because of the quasigrating sidewall corrugation in the ring resonator, mutual-coupling is induced between the clockwise and counterclockwise modes [36]. It was already found that the mutual coupling strength is proportional to the reflectivity of the quasigratings and the resonance splitting occurs if the reflectivity is high [31]. However, the resonance splitting is uncontrollable since the mutual coupling relies on random perturbations along the ring sidewall. In this paper, we propose a silicon microring modulator based on controlled mutual coupling without taking into account the sidewall corrugation induced grating effect. The device consists of a double-waveguide coupled racetrack ring resonator embedded with a grating, which is formed by etching periodic holes on part of the racetrack ring. By setting a p-i-n diode along the grating, optical intensity modulation can be achieved by shifting the grating spectrum via the FCD effect, which changes the grating reflectivity and hence the mutual coupling strength. The modulation depth of the proposed modulator is determined by the tunable range of the grating reflectivity. Therefore, high modulation depth can be realized by increasing the tuning range of the grating reflectivity. For a specifically designed grating with a length of 6.5 μm, modulation depth of ~10 dB can be obtained when the carrier density change is ~5.5×10^{17} cm^{-3}. Compared with the smallest demonstrated silicon microring modulator with a ring radius of 2.5 μm and carrier density change of ~3.9×10^{17} cm^{-3} [12], the required total charge

injection reduces by ∼40% in our proposed modulator due to the smaller volume of the p-i-n region along the grating. Therefore, low energy consumption is achievable. As the modulation is carried out by changing the transmission at the unshifted resonances and the phase variation induced by the grating spectrum shift is negligible, low-chirp modulation can be expected. Compared with the coupling-tuning based silicon ring modulators employing long MZI arms, the proposed modulator is more compact since the grating is embedded within the microring waveguide. Unlike MZI based modulators, the proposed modulator has back reflection induced by the grating, which may cause destabilization of laser source. Therefore, an optical isolator is required before the modulator to eliminate the undesirable feedback.

Table 1 summarizes the device performance for several silicon microring modulators including forward-biased p-i-n based modulators [37], reverse-biased modulators [13,38], differentially signaled modulators [39], and the device presented in this work. Frequency chirp is also an important parameter to evaluate modulator performance. For the resonance-shift based microring resonators, the frequency chirp is usually of the order of 10 GHz [13,37,38]. In comparison, less than 1 GHz frequency chirp is obtained in our proposed structure.

2. DEVICE DESCRIPTIONS

The schematic of the proposed device is shown in Fig. 1. It consists of a silicon racetrack microring resonator embedded with an electrically tunable grating on a silicon-on-insulator (SOI) platform with a 3 μm-thick buried oxide layer. The bending radius of the racetrack microring is $r = 5$ μm. The bus and ring rib waveguides have a typical width of 0.5 μm, a height of 0.25 μm, and a 50 nm-thick slab for p- and n-type doping along the grating. Very tight waveguide bends with radii down to a few micrometers can be realized with this waveguide geometry [11]. The device is clad with a 1 μm-thick silicon dioxide layer. The grating is essentially a one-dimensional photonic crystal waveguide with circular holes, as shown in Fig. 2(a). The hole radius is denoted as R_h, and the holes are etched through the silicon layer with a depth of $D = 250$ nm. The grating length L is of several micrometers. The grating period is assumed to be 310 nm and the grating has the same width as the rib waveguide. The doping profile of the grating waveguide is similar to that of the p-i-n diode in silicon microring modulators [9]. Figures 2(b) and 2(c) show the cross sections of the grating segments without and with circular holes, respectively. The distance between the doped regions and the edge of the grating is 300 nm. The widths of the p- and

Table 1. Comparison of Previously Demonstrated Silicon Microring Modulators and the Proposed Modulator

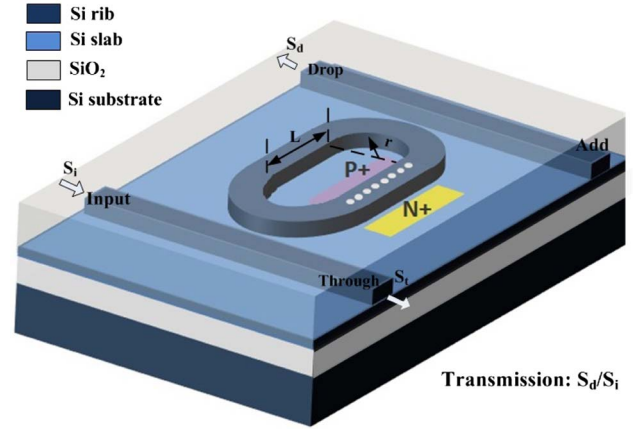|	Modulation Depth (dB)	Speed (Gb/s)	Power (fJ/bit)	Device Length (μm)	References
Cornell	3	18	∼300	12	[37]
Kotura	6.5	12.5	50	30	[13]
Oracle	5	25	7	15	[38]
Sandia	5	10	3	3.5	[39]
Proposed structure	13	10	122.5	∼20	

Fig. 1. (Color online) Schematic of the tunable resonance-splitting based silicon ring modulator.

n-doping regions are both 600 nm with a doping concentration of 1×10^{19} cm^{-3}.

3. OPERATION PRINCIPLE OF THE TUNABLE-GRATING-BASED SILICON RING MODULATOR

A. Definition of Contrast Factor F

We first present the working principle of the tunable grating based silicon microring modulator. By modifying the grating parameters, such as period, width, and duty cycle, the effective refractive index of the grating can be engineered, while the grating reflection spectrum can shift with the effective index change. We define a reflectivity contrast factor $F = (R_1/R_2)^{1/2}$ to evaluate the reflectivity change induced by the grating spectrum shift, where R_1 and R_2 correspond to the reflectivity before and after the spectrum shift, respectively. We assume that the coupling coefficients between both the bus waveguides and the ring are the same, which is denoted as κ. Based on the analysis for microring resonators with surface corrugation [36], resonance splitting begins to appear when the reflectivity R is comparable to κ^4. When $R \ll \kappa^4$, there is no resonance splitting, and a transmission peak can be obtained at the resonant wavelength in the drop channel. When $R \gg \kappa^4$, the resonance is strongly split, resulting in a transmission dip at the resonant wavelength. We choose the coupling coefficient κ to satisfy $\kappa^4 = \sqrt{R_1 R_2}$ and $R_1 > \kappa^4 > R_2$. In this case, the transmission contrast at the resonance wavelength increases with F, and hence optical modulation with a high extinction ratio is achievable.

We then analytically investigate the spectral responses around the ring resonance to study the dependency of modulation depth on F. Using steady-state transfer equations, one can express the spectral response of the drop channel as [31]:

$$T_d = \frac{S_d}{S_i} = -j \frac{\kappa^2}{1 - t^2 G a \, \exp(-j\varphi)}, \tag{3a}$$

$$G = \frac{t_r - (1 - A_L)t^2 a \, \exp(-j\varphi)}{1 - t_r t^2 a \, \exp(-j\varphi)}, \tag{3b}$$

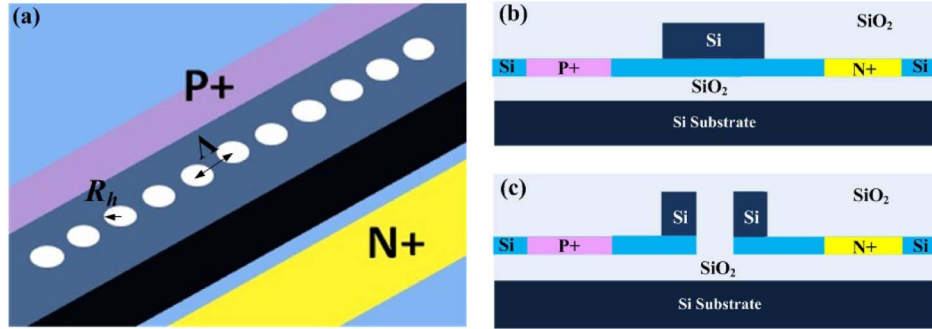$$\varphi = 2\pi[n_{\text{eff},r}(L_R - L) + n_{\text{eff},g}L]/\lambda, \tag{3c}$$

Fig. 2. (Color online) (a) Schematic of the grating structure. (b) and (c) Schematic cross sections of the grating segments (b) without circular hole and (c) with circular hole.

$$a = \exp[-\alpha(L_R - L)], \tag{3d}$$

where L_R is the total length of the racetrack microring resonator and φ is the phase change after one round-trip of the ring. $t = \sqrt{1 - \kappa^2}$ is the transmission coefficient associated with κ, a denotes the single-pass amplitude transmission in the ring waveguide with the propagation loss factor α, and $t_r = \sqrt{1 - A_L - R}$ is grating field transmission dependent on the grating reflectivity R and the grating loss A_L. $n_{\mathrm{eff},r}$ and $n_{\mathrm{eff},g}$ are the effective indices of microring and grating waveguides for TE mode, respectively. Based on waveguide eigenmode simulations, we get $n_{\mathrm{eff},r} = 2.57$ and $n_{\mathrm{eff},g} = 2.2$. $n_g = 4.2$ is the group index of the ring waveguide obtained from our previous experimental results [31]. Since A_L dominates the total loss in the racetrack ring, we set $a = 1$ in the following calculations. The extinction ratio of the proposed modulator is defined as

$$\mathrm{ER} = 10 \lg \left| \frac{T_{d2}}{T_{d1}} \right|^2, \tag{4}$$

where T_{d1} corresponds to a transmission dip with $R = R_1$ at the resonant wavelength ($\varphi = 0$). When $R = R_2$, a transmission peak T_{d2} is obtained, which also determines the insertion loss of the modulator. It should be noted that there is a resonant wavelength misalignment of $\Delta\lambda = \Delta n_{\mathrm{eff},g}\lambda L/(n_g L_R)$ between T_{d1} and T_{d2}, which is induced by the grating effective index change $\Delta n_{\mathrm{eff},g}$. However, the small misalignment has little effect on the modulator performance, which will be explained in the following part.

B. Dependency of Modulation Depth on F

The modulation depth and insertion loss of the modulator are plotted as a function of κ with different F in Fig. 3. To explore the influence of grating loss on the performance of the proposed modulator, we consider four cases with $A_L = 0.01$, $A_L = 0.02$, $A_L = 0.05$, and $A_L = 0.1$. As A_L becomes larger with other parameters unchanged, the modulation depth decreases while the insertion loss increases, as shown in Fig. 3. The increase of A_L leads to a lowered quality factor Q of the resonator system. As a result, resonance splitting is weakened
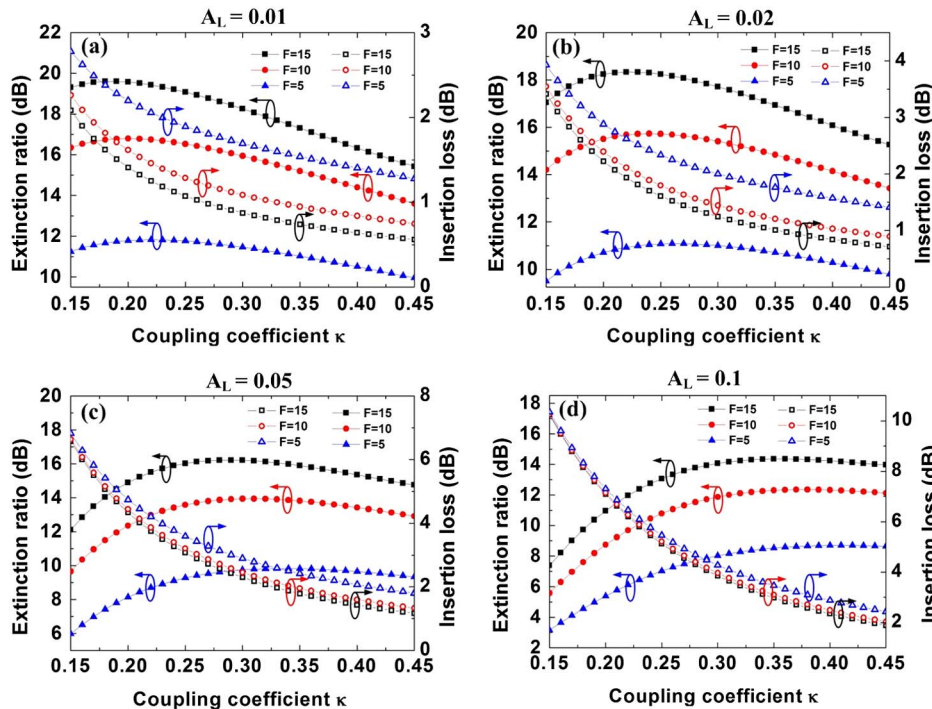

Fig. 3. (Color online) Modulation depth as a function of coupling coefficient κ with (a) $A_L = 0.01$, (b) $A_L = 0.02$, (c) $A_L = 0.05$, and (d) $A_L = 0.1$.

and the transmission dip becomes shallow. Meanwhile, the transmission peak becomes lower with the reduction in Q, leading to a higher insertion loss. For $A_L = 0.01$, $A_L = 0.02$, and $A_L = 0.05$, a modulation depth of ~10 dB can be obtained when $F \geq 5$. With A_L increases to 0.1, $F \geq 10$ is required to achieve a modulation depth of ~10 dB, as shown in Fig. 3(d). When $A_L = 0.01$, the extinction ratio of the modulator can reach ~20 dB with an insertion loss of less than 1 dB. For $A_L = 0.02$ and $A_L = 0.05$, $\kappa > 0.19$ and $\kappa > 0.25$ are required respectively to ensure that the insertion loss is lower than 3 dB with $F = 5$. When $A_L = 0.1$, $\kappa > 0.35$ is required with $F = 10$. Therefore, a small A_L and a large F are desired to achieve a high modulation depth and a low insertion loss with less restriction on κ.

Because of the scattering and radiation losses in gratings, it is hard to obtain near-zero reflectivity. We show in the following simulations that the minimal reflectivity and loss are $R_2 = 1.6 \times 10^{-3}$ and $A_L = 0.04$, respectively. Since $F \geq 5$ is required to realize 10 dB modulation depth for $A_L = 0.04$, $\Delta R = R_2(F^2 - 1) \approx 0.04$ is the minimal reflectivity change to obtain a 10 dB modulation depth. In the following simulations, the grating length L and the radius of the circular holes R_h are varied to obtain $\Delta R \geq 0.04$ with a certain spectrum shift.

4. SIMULATION RESULTS AND DISCUSSION

A. Carrier Injection Induced Refractive Index Change and Grating Spectrum Shift

As the grating is electrically tuned by the p-i-n diode, we first investigate the carrier injection induced refractive index change. To simulate the carrier-concentration variation in the grating waveguide when applied with forward bias voltage across the p-i-n diode, we use commercial electronic device simulator ATLAS by Silvaco including Shockley Read Hall, Auger, and direct recombination models. We assume an interface trap density of $10^{10}/cm^2/eV$ and an interface recombination rate of 10^4 cm/s. The surface recombination rate of silicon is in the order of 10^4 cm/s for unpassivated surfaces. Soref's expressions [40,41] are used to determine the carrier-induced refractive index change Δn and absorption loss $\Delta \alpha$ at 1.55 μm wavelength in silicon. When operating in an optimum charge injection level with a bias voltage of 1.13 V, a drive voltage $V_{pp} = 540$ mV can induce a relatively large change in carrier concentration of ~5.5×10^{17} cm^3, corresponding to a refractive index change $\Delta n = -1.8 \times 10^{-3}$, as shown in
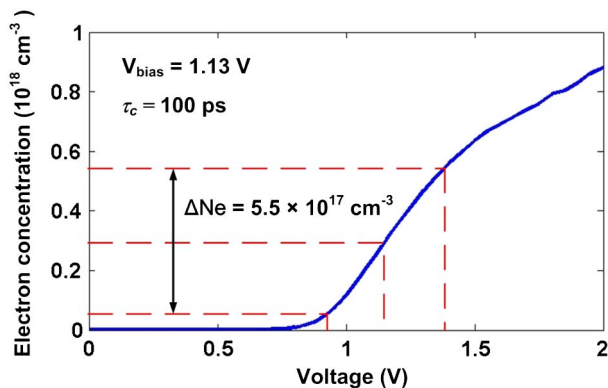
Fig. 4. The voltage drop on the junction of the p-i-n diode changes from 0.07 to 0.43 V when the applied voltage increases from 0.86 to 1.4 V. At the bias voltage of 1.13 V, the voltage drop is 0.16 V. In the following analysis, we use $\Delta n = -1.8 \times 10^{-3}$ to simulate the grating spectrum shift. The free carrier induced absorption loss of 0.02 dB is negligible since the scattering loss induced by the grating dominates.

We then investigate the reflectivity change ΔR with respect to the spectrum-shift $\Delta \lambda$. The grating reflectivity $R(\lambda)$ is a function of wavelength λ, and the reflectivity change due to its spectrum shift can be expressed as $\Delta R = R(\lambda) - R(\lambda + \Delta \lambda)$. The reflectivity contrast factor F reaches the maximum at the spectral dip between the main lobe and the first-order sidelobe with a certain $\Delta \lambda$. Therefore, the reflectivity change at the spectral dip, defined as ΔR_m, is investigated. With $\Delta n = -1.8 \times 10^{-3}$, the overall effective refractive index change $\Delta n_{\text{eff},g}$ is obtained by simulating the mode profiles of each grating segment. To provide an estimation, circular holes can be approximated by square-shaped holes with a side length of $L_s = 2R_h$. The obtained refractive index change is $\Delta n_{\text{eff},g2} = -1.15 \times 10^{-3}$ for the grating segments with $L_s = \sim 100$ nm, while $\Delta n_{\text{eff},g1} = -1.55 \times 10^{-3}$ is obtained for the grating segments without holes. The optical confinement factors for the grating segments with and without hole are ~0.45 and ~0.82, respectively. The effective refractive index change then can be calculated as $\Delta n_{\text{eff},g} = (\Delta n_{\text{eff},g1}(\Lambda - L_s) + \Delta n_{\text{eff},g2}L_s)/\Lambda$ and the spectrum shift $\Delta \lambda = 2\Delta n_{\text{eff},g}\Lambda$. The variation of ΔR_m as a function of grating length L for different L_s's is illustrated based on the equations for the spectral responses of grating reflectivity [42]. Figure 5 shows that ΔR_m increases monotonically with grating length L and slightly increases when L_s increases from 100 nm to 150 nm. $\Delta R_m = 0.04$ is achieved when $L = 6.5$ μm.

B. Optical Responses of the Grating Structures

To verify the above estimation, we simulate spectral responses of the grating structure using Lumerical three dimension (3D) finite-difference time-domain (FDTD) solutions. All simulations were carried out on a layout size of $x \times y \times z = 3 \times 10 \times 3$ μm^3 with a mesh resolution of $\Delta x \times \Delta y \times \Delta z = 10 \times 10 \times 10$ nm^3. Material refractive indices are $n_{\text{Si}} = 3.477$ and $n_{\text{SiO2}} = 1.445$, respectively. The simulation time step is 1.86×10^{-17} s according to the Courant

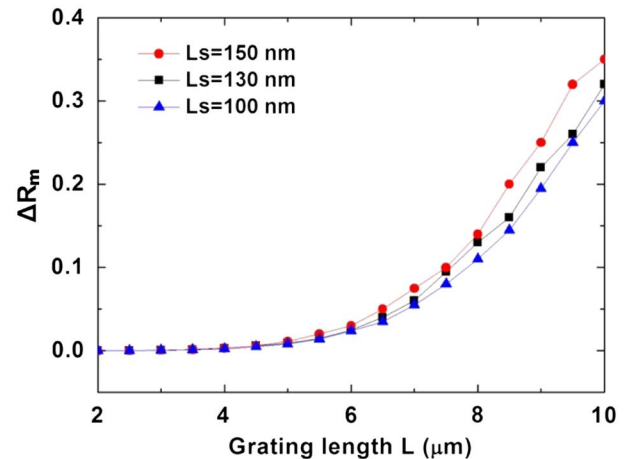Fig. 4.   (Color online) Carrier injection efficiency of the p-i-n diode in the proposed modulator.

Fig. 5.   (Color online) Reflectivity change ΔR as a function of grating length L.

criterion $\Delta t \le 1/[c(1/\Delta x^2 + 1/\Delta y^2 + 1/\Delta z^2)^{1/2}]$, where c is the speed of light in vacuum. The Si wire waveguide mode with TE polarization is used to excite the Bloch mode in the grating with a wavelength range from 1550 to 1650 nm.

The grating structure with $L = 6.5$ μm, $\Lambda = 310$ nm, and $R_h = 65$ nm is simulated since $\Delta R_m = {\sim}0.04$ can be obtained according to Fig. 5. The grating loss is $A_L = 0.04$ and $\Delta R_m = R_1 - R_2 = 0.039$ is obtained when the spectrum has a blue-shift of $\Delta \lambda = 0.896$ nm with an applied voltage of $V_{pp} = 0.54$ V, as shown in Fig. 6(a). As a result, $F = 5.2$ is achieved at the minimum reflection point $R_2 = 1.6 \times 10^{-3}$ between the main lobe and the first-order sidelobe. When R_h increases to 75 nm, the maximal F reaches 6.2 with the corresponding $\Delta R_m = 0.042$, as shown in Fig. 6(b). Comparing the grating spectra in Figs. 6(a) and 6(b), one can see that the rising/falling edges in the grating spectrum become sharper as R_h increases from 65 to 75 nm. We also investigate the grating spectrum shift when the grating length increases to 7.5 μm with $R_h = 65$ nm [Fig. 6(c)] and 75 nm [Fig. 6(d)], respectively. The rising/falling edges in the grating spectrum become steeper leading to higher contrast factors of $F = 7.5$ ($R_h = 65$ nm) and $F = 8.2$ ($R_h = 75$ nm). Transmission and reflectivity as a function of applied bias and carrier density at the resonant wavelength are also investigated for the grating with $L = 7.5$ μm and $R_h = 65$ nm, presenting the dynamic variation of the grating spectrum, as shown in Fig. 7. Table 2 summarizes the design parameters and variables used in the above four different grating structures.

C. Modulation Depth and Insertion Loss of the Modulator

Based on Eq. (3), one can numerically calculate the spectral responses of the ring resonator incorporating the grating performance from the above simulations. Initially, the circumference of the racetrack ring is adjusted such that the ring resonance occurs exactly at the reflection point R_1. With the drive voltage increases by 540 mV, the grating spectrum blue-shifts; thus the grating reflectivity varies from R_1 to R_2 at the ring resonant wavelength. Figure 8 displays the periodic responses of ring resonators with different grating parameters in both the through port and drop port. When the drive voltage is applied, it can be seen that the optical response of each resonator only significantly changes around one resonance in the wavelength range of 60 nm, implying that the grating reflectivity varies drastically at that point. The drop channel spectra around the drastically varied resonances are plotted in Fig. 9. As shown in Fig. 9(a), a transmission dip of ${\sim}{-}12$ dB is achieved at the resonant wavelength with $R_1 = 0.04$, which corresponds to grating parameters of $L = 6.5$ μm and $R_h = 65$ nm. A transmission peak of ${\sim}{-}2.8$ dB is obtained when the ring resonance occurs at $R_2 = 1.6 \times 10^{-3}$. A modulation depth of ${\sim}9.2$ dB is achieved with an insertion loss of ${\sim}{-}2.8$ dB. Similarly, a modulation depth of ${\sim}10.5$ dB is obtained when $R_h = 75$ nm, as illustrated in Fig. 9(b). For $L = 7.5$ μm, since the achieved F values are larger than those for $L = 6.5$ μm, the corresponding modulation depth increases to ${\sim}13$ dB [Fig. 9(c)] and ${\sim}14$ dB [Fig. 9(d)] for $R_h = 65$ nm and $R_h = 75$ nm, respectively. The phase responses of
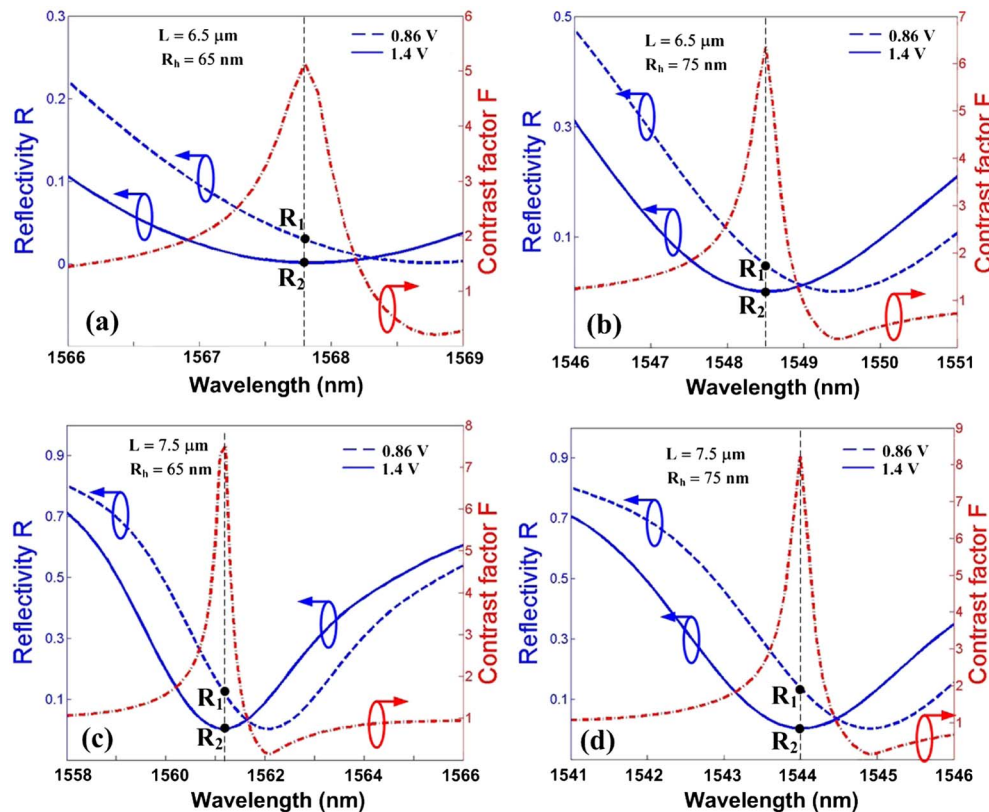

Fig. 6. (Color online) Simulated grating reflectivity and contrast factor with (a) $L = 6.5$ μm and $R_h = 65$ nm, (b) $L = 6.5$ μm and $R_h = 75$ nm, (c) $L = 7.5$ μm and $R_h = 65$ nm, and (d) $L = 7.5$ μm and $R_h = 75$ nm.
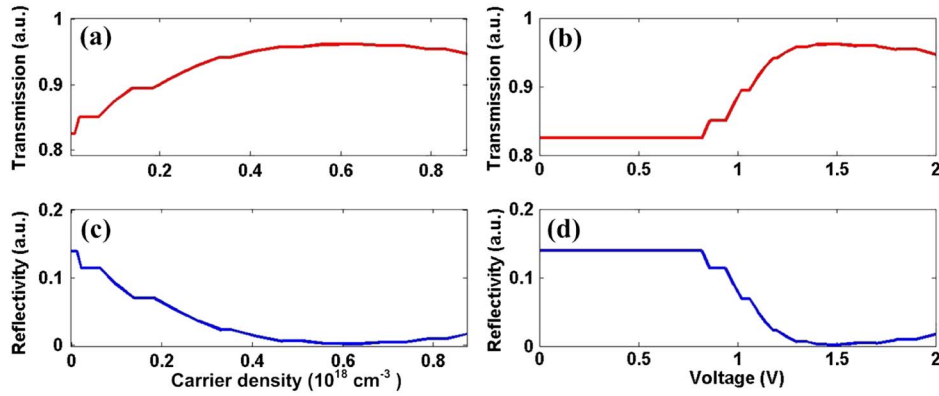
Fig. 7.   (Color online) Transmission as a function of (a) carrier density and (b) applied voltage, and reflectivity as function of (c) carrier density, and (d) applied voltage with $L = 7.5$ μm and $R_h = 65$ nm.

the resonators are also plotted in Fig. 9. Different phase properties are obtained with the drive voltage change. Nevertheless, little phase variation occurs at the resonant wavelength for all the four cases, implying a low-chirp intensity modulation. With the applied drive voltage, there is a resonance shift $\Delta\lambda$ due to the carrier injection, and the impact of the resonance shift on the modulation is investigated. Based on $\Delta\lambda = \Delta n_{\text{eff},g}\lambda L/(n_g L_R)$, $\Delta\lambda = \sim 0.08$ nm is obtained and the induced modulation depth variation is ~ 0.1 dB, which is negligible. Based on $\kappa = (R_2 F)^{1/4}$ derived from the above definitions, the increase of F leads to a higher coupling coefficient κ, and hence lower optical quality factor Q. Figure 10 shows the individual optical responses of the Bragg reflector and ring resonator, as well as the proposed structure in a wavelength range of 100 nm for two proposed modulators with different grating parameters. It can be seen that both the bandgap of the Bragg reflector and the quality factor of the ring resonator are smaller for a longer grating, resulting in steeper rising/falling edges of grating spectrum and wider 3 dB resonance bandwidths. Therefore, larger reflectivity variation occurs around the ring resonance in the modulator with a longer grating, leading to more distortion even though the resonant wavelength matches the minimum reflection point, as shown in Fig. 10(b).

In practice, exact alignment between the ring resonance and the minimum reflection point is hard to realize. If the ring resonance mismatches the grating minimum reflection point R_2, reflection contrast factor F is lowered. Figure 11 shows the degraded modulator performances as the modulation depth decreases [Fig. 11(a)] and the insertion loss increases [Fig. 11(b)] with the misalignment. When the resonant wavelength blue-shifts, F slightly decreases, resulting in a slow reduction of the modulation depth. However, the insertion loss increases significantly as the minimum reflectivity becomes higher than R_2. With the resonant wavelength red-shifts, fast

reduction of F is obtained, and as a result, the modulation depth decreases rapidly. Figure 11 also shows that the variation slopes for both the modulation depth and the insertion loss become steeper as the grating length and hole radius increase. The tolerance for the resonance mismatch is around ± 0.2 nm to maintain a high modulation performance. In practice, the mismatch can be compensated for by thermally shifting the ring resonance, which can be achieved by inserting a thin-film titanium micro-heater on top of the ring resonator. As shown in Fig. 12, the titanium microheater with multiwire structure [43,44] is isolated by trenches [45,46] and covers only part of the racetrack ring waveguide with the same length as grating to reduce thermal crosstalk.

In order to show that the proposed modulator has good tolerance to the resonator coupling variation, we also discuss the modulation depth as a function of coupling coefficient κ for various grating parameters illustrated in Fig. 13. As shown in Figs. 13(a) and 13(b), both the modulation depth and the insertion loss of the modulator decrease with the increase of κ. Figure 13(a) shows that a modulation depth of greater than 10 dB can be obtained when $\kappa < 0.29$ in the case of $L = 6.5$ μm and $R_h = 75$ nm. To keep the insertion loss lower than 3 dB, $\kappa > 0.27$ is required as shown in Fig. 13(b). As the grating length increases to 7.5 μm, a modulation depth of larger than 10 dB can be obtained with $\kappa < 0.42$, while $\kappa > 0.29$ is required to ensure that the insertion loss is lower than 3 dB. Therefore, the tolerance on κ is enhanced with the increase of grating length, which is essentially due to the increase in F. With a fixed κ, the modulation depth can be tuned by varying F, while the corresponding insertion loss is only slightly changed. In particular, the modulation depth increases from 9.7 to 15.3 dB as F changes from 6.2 to 7.5 with $\kappa = 0.3$. The insertion loss is varied within ~ 0.25 dB. In addition, F can also be improved by increasing the drive voltage V_{pp} to induce a larger spectrum shift, leading to enhancement of the modulation depth.

D. Bandwidth and Energy Consumption

As a forward-biased p-i-n diode is applied in the proposed device, the 3 dB bandwidth is mainly determined by the free carrier lifetime τ_c and the cavity photon lifetime τ_p. The effective carrier lifetime $\tau_c = 100$ ps can be obtained by using carrier lifetime reduction scheme [47], allowing for a 3 dB bandwidth of 10 GHz, as shown by the red solid line in Fig. 14. To estimate the influence of τ_p on the device bandwidth, we use the

Table 2.   Design Parameters and Variables of Four Grating Structures

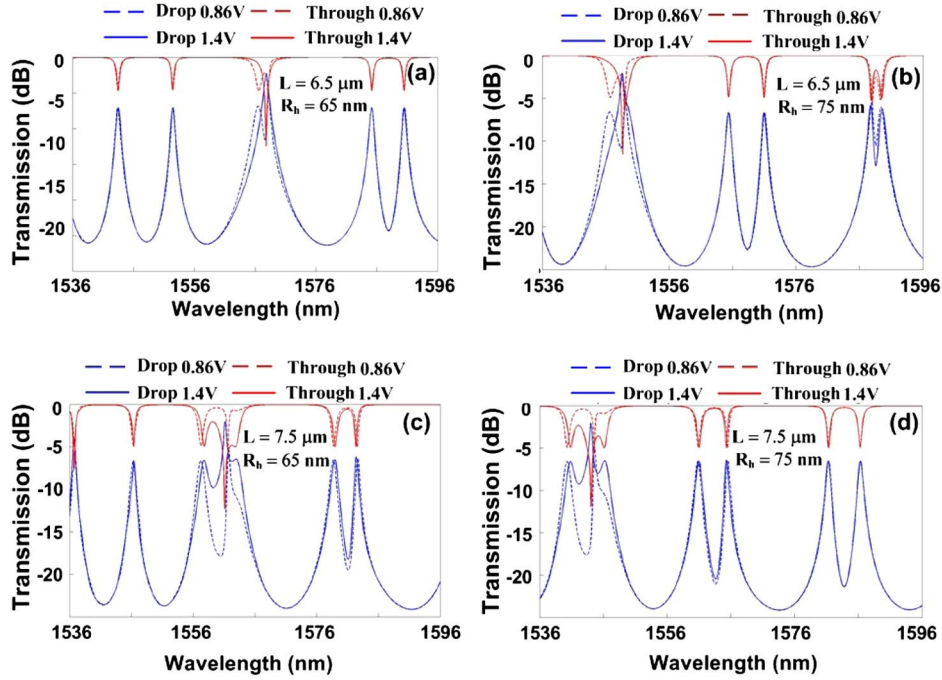| L (μm)	R_h (nm)	Δn_{eff}	$\Delta\lambda$ (nm)	ΔR	F
6.5	65	1.38E − 3	0.856	0.039	5.2
6.5	75	1.31E − 3	0.812	0.042	6.2
7.5	65	1.38E − 3	0.856	0.112	7.5
7.5	75	1.31E − 3	0.812	0.134	8.2

Fig. 8. (Color online) Periodic responses of ring resonators with different grating parameters (a) $L = 6.5$ µm and $R_h = 65$ nm, (b) $L = 6.5$ µm and $R_h = 75$ nm, (c) $L = 7.5$ µm and $R_h = 65$ nm, and (d) $L = 7.5$ µm and $R_h = 75$ nm in both the through port and drop port.

equation $f_{3\text{ dB}} = c/(\lambda Q)$, derived from $\tau_p = \lambda Q/(2\pi c)$ and $f_{3\text{ dB}} = 1/(2\pi\tau_p)$ [11], where c is the light speed in vacuum. The intrinsic quality factor Q_0 is determined by the effective propagation loss of the ring and can be estimated as follows:

$$\alpha_{\text{eff}} = \frac{\alpha(L_R - L) - \ln(1 - A_L)}{L_R} \text{ (nep/m)}, \qquad (5)$$

where $\alpha = 0.7$/cm, based on previous experiments [48]. $A_L = 0.04$ and $L_R = 2\pi r + 2L = 46.4$ µm are obtained with
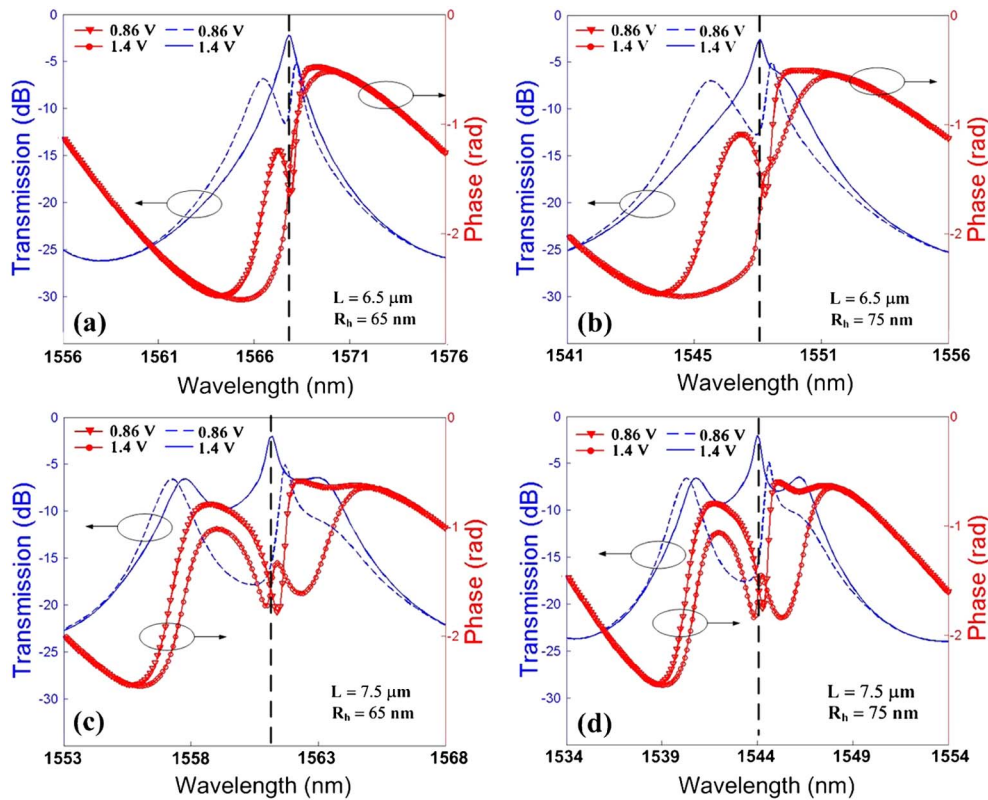

Fig. 9. (Color online) Spectral responses of the proposed modulator for grating parameters of (a) $L = 6.5$ µm and $R_h = 65$ nm, (b) $L = 6.5$ µm and $R_h = 75$ nm, (c) $L = 7.5$ µm and $R_h = 65$ nm, and (d) $L = 7.5$ µm and $R_h = 75$ nm.
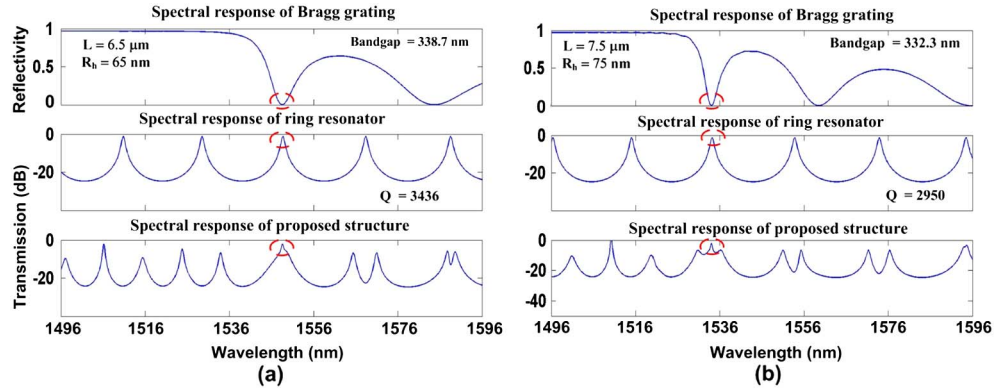
Fig. 10.   (Color online) Optical responses of the Bragg reflector and ring resonator, as well as the proposed structure in a range of 100 nm with different grating parameters of (a) $L = 6.5$ μm and $R_h = 65$ nm and (b) $L = 7.5$ μm and $R_h = 75$ nm.
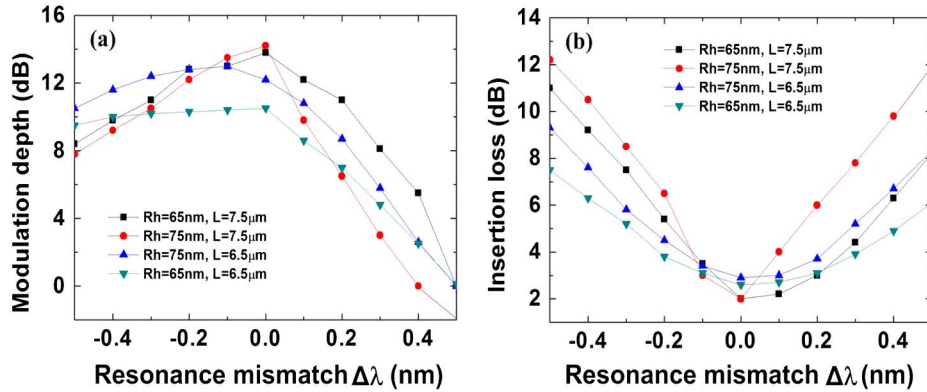

Fig. 11.   (Color online) Influence of the resonance mismatch $\Delta\lambda$ on (a) modulation depth and (b) insertion loss.

$L = 7.5$ μm. Thus, $Q_0 = 18550$ is obtained as $Q_0 = 2\pi n_g/(\alpha_{\rm eff}\lambda)$ and the external quality factor Q_e is related with κ as $Q_e = \pi L_R n_g/(\kappa^2 \lambda)$ [49]. The total loaded quality factor is given by $Q = Q_0 Q_e/(Q_0 + Q_e)$. We plot the 3 dB bandwidth of the modulator as a function of κ (blue dashed curve in Fig. 14). When $\kappa < 0.35$, the 3 dB bandwidth is determined by τ_p and increases as κ increases. A 3 dB bandwidth of 10 GHz is obtained with $\kappa = 0.35$. The corresponding modulation depth and insertion loss are 13 dB and 1.9 dB, respectively, as shown in Fig. 13. When $\kappa > 0.35$, optical modulation bandwidth is limited by τ_c and the achievable maximal value is 10 GHz.

Low power operation in optical modulators is of particular importance for large-scale on-chip integration. The dynamic energy consumption of the proposed modulator is estimated by calculating the switching energy per carrier injection, which is defined as the total charge injected to the p-i-n diode times voltage swing [12]. It should be noted that this estimation provides the minimum required energy for modulation without considering the energy consumption induced by external wiring, such as contact resistance and capacitance. In this case, the energy consumption can be given by the following equation:

$$\text{Energy/bit} = 1/4 \times e \times (\Delta N_e + \Delta N_h) \times \text{Volume} \times V_{pp}, \quad (6)$$

where e is the electron charge, Volume $= S_{\rm modal_area} \times L$ is the modal volume of the grating section with an effective modal area of $S_{\rm modal_area} = 0.125$ μm^2, V_{pp} is the peak-to-peak drive

voltage, and ΔN_e and ΔN_h are the injected electron- and hole-density, respectively. Since the 0–1 transition only happens with a probability of 0.25 for all bit sequences [50], the coefficient of 1/4 is included. A drive voltage of $V_{pp} = 540$ mV corresponds to $\Delta N_e = \Delta N_h = 5.5 \times 10^{17}$ cm^{-3}. The resulting dynamic energy consumption is 22 fJ/bit with a grating length $L = 7.5$ μm. The DC power consumption of the proposed modulator is approximately given by $P_{\rm DC} = V_{\rm on} I_{\rm on}$ [12], where $I_{\rm on} = e \times \rho \times \text{volume}/\tau_c = \sim 0.89$ mA with $\tau_c = 100$ ps, $\rho = 2.8 \times 10^{17}$ cm^{-3} is the steady state carrier density at the bias voltage of $V_{\rm on} = 1.13$ V. At a modulation speed of 10 Gb/s, the average DC power consumption is
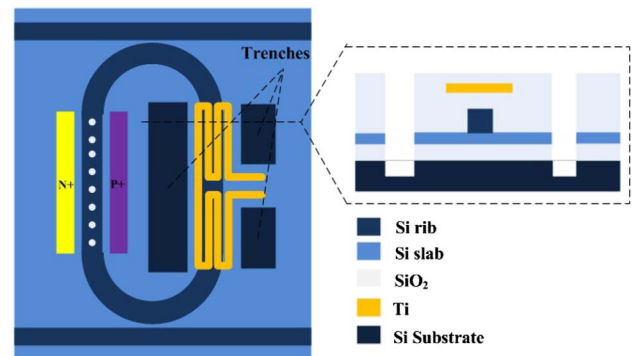

Fig. 12.   (Color online) Schematic of the titanium micro-heater structure for compensating the mismatch between the ring resonance and the minimum reflection point.
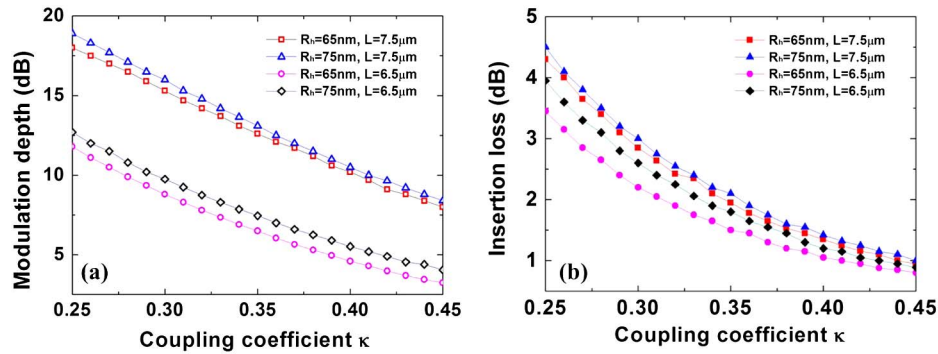
Fig. 13. (Color online) (a) Simulated modulation depth and (b) insertion loss as functions of κ for various L's and L_s's.
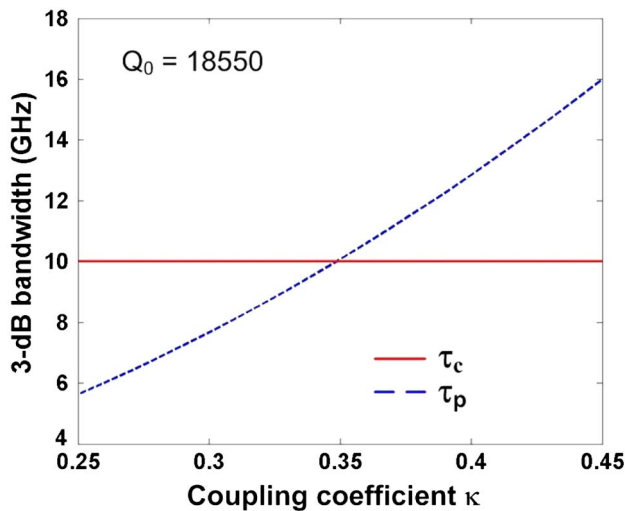

Fig. 14. (Color online) Theoretical calculation of the 3 dB bandwidth as a function of κ considering the limiting factors of free carrier lifetime τ_c and photon lifetime τ_p.

100.3 fJ/bit. The total energy consumption of the modulator is 122.3 fJ/bit.

When there is a mismatch between the ring resonance and the minimum reflection point, extra power consumption is required for thermally shifting the resonance. It has been experimentally demonstrated that the resonance tuning efficiency can achieve ~19 mW/THz for a single-ring resonator [43]. Since the titanium microheater covers only part of the racetrack ring waveguide, the tuning efficiency in our structure would be ~129.8 mW/THz. It should be noted that the thermal tuning power consumption can be reduced or even eliminated by using cutting-edge device fabrication processes with high accuracy.

5. CONCLUSION

We proposed a silicon racetrack ring modulator based on mutual mode coupling tuning. By introducing an electrically tuned grating inside the ring, a transmission switch between a peak and a dip occurs at the resonant wavelength in the drop channel, enabling optical intensity modulation. The modulation depth can be enhanced by increasing the grating length or drive voltage, regardless of the coupling condition of the ring resonator. In particular, a modulation depth of ~13 dB can be obtained with a moderate insertion loss of 1.9 dB,

low energy consumption of 122.3 fJ/bit, and a 3 dB bandwidth of 10 GHz, based on 3D FDTD simulations.

REFERENCES

1. D. A. B. Miller, "Optical interconnects to silicon," IEEE J. Sel. Top. Quantum. Electron. **6**, 1312–1317 (2000).
2. J. D. Meindl, J. A. Davis, P. Zarkesh-Ha, C. S. Patel, K. P. Martin, and P. A. Kohl, "Interconnect opportunities for gigascale integration," IBM J. Res. Dev. **46**, 245–263 (2002).
3. A. Liu, R. Jones, L. Liao, D. Samara-Rubio, D. Rubin, O. Cohen, R. Nicolaescu, and M. Paniccia, "A high-speed silicon optical modulator based on a metal-oxide-semiconductor capacitor," Nature **427**, 615–618 (2004).
4. L. Liao, D. Samara-Rubio, M. Morse, A. Liu, D. Hodge, D. Rubi, U. D. Keil, and T. Franck, "High speed silicon Mach-Zehnder modulator," Opt. Express **13**, 3129–3135 (2005).
5. A. Huang, G. Li, Y. Liang, S. Mirsaidi, A. Narasimha, T. Pinguet, and C. Gunn, "A 10 Gb/s photonic modulator and WDM MUX/DEMUX integrated with electronics in 0.13 μm SOI CMOS," presented at the IEEE International Solid-State Circuits Conference, San Francisco, CA, USA, 2006.
6. K. Ogawa, K. Goi, Y. T. Tan, T. Liow, X. Tu, Q. Fang, G. Lo, and Dim-Lee Kwon, "Silicon Mach-Zehnder modulator of extinction ratio beyond 10 dB at 10.0–12.5 Gbps," Opt. Express **19**, B26–B31 (2011).
7. R. A. Soref and J. P. Lorenzo, "All-silicon active and passive guided-wave components for $\lambda = 1.3$ and 1.6 μm," IEEE J. Quantum Electron. **22**, 873–879 (1986).
8. R. A. Soref and B. R. Bennett, "Electrooptical effects in silicon," IEEE J. Quantum Electron. **23**, 123–129 (1987).
9. Q. Xu, B. Schmidt, S. Pradhan, and M. Lipson, "Micrometre-scale silicon electro-optic modulator," Nature **435**, 325–327 (2005).
10. Q. Xu, S. Manipatruni, B. Schmidt, J. Shakya, and M. Lipson, "12.5 Gbit/s carrier-injection-based silicon microring silicon modulators," Opt. Express **15**, 430–436 (2007).
11. P. Dong, S. Liao, D. Feng, H. Liang, D. Zheng, R. Shafiiha, C. Kung, W. Qian, G. Li, X. Zheng, A. Krishnamoorthy, and M. Asghari, "Low Vpp, ultralow-energy, compact, high-speed silicon electro-optic modulator," Opt. Express **17**, 22484–22490 (2009).
12. S. Manipatruni, K. Preston, L. Chen, and M. Lipson, "Ultra-low voltage, ultra-small mode volume silicon microring modulator," Opt. Express **18**, 18235–18242 (2010).
13. P. Dong, R. Shafiiha, S. Liao, H. Liang, N. N. Feng, D. Feng, G. Li, X. Zheng, A. V. Krishnamoorthy, and M. Asghari, "Wavelength-tunable silicon microring modulator," Opt. Express **18**, 10941–10946 (2010).
14. P. Dong, S. Liao, H. Liang, W. Qian, X. Wang, R. Shafiiha, D. Feng, G. Li, X. Zheng, A. V. Krishnamoorthy, and M. Asghari,

"High-speed and compact silicon modulator based on a racetrack resonator with a 1 V drive voltage," Opt. Lett. **35**, 3246–3248 (2010).

15. W. A. Zortman, A. L. Lentine, M. R. Watts, and D. C. Trotter, "Power penalty measurement and frequency chirp extraction in silicon microdisk resonator modulators," in *Optical Fiber Communication Conference*, Technical Digest (CD) (Optical Society of America, 2010), paper OM17.

16. A. Biberman, S. Manipatruni, N. Ophir, L. Chen, M. Lipson, and K. Bergman, "First demonstration of long-haul transmission using silicon microring modulators," Opt. Express **18**, 15544–15552 (2010).

17. A. M. Gutierrez, A. Brimont, G. Rasigade, M. Ziebell, D. Marris-Morini, J.-M. Fédéli, L. Vivien, J. Marti, and P. Sanchis, "Ring-assisted Mach–Zehnder interferometer silicon modulator for enhanced performance," J. Lightwave Technol. **30**, 9–14 (2012).

18. A. Yariv, "Critical coupling and its control in optical waveguide-ring resonator systems," IEEE Photon. Technol. Lett. **14**, 483–485 (2002).

19. W. D. Sacher and J. K. S. Poon, "Characteristics of microring resonators with waveguide-resonator coupling modulation," J. Lightwave Technol. **27**, 3800–3811 (2009).

20. M. A. Popovic, "Resonant optical modulators beyond conventional energy-efficiency and modulation frequency limitations," in *Integrated Photonics Research, Silicon and Nanophotonics* (Optical Society of America, 2010), paper IMC2.

21. T. Ye, Y. Zhou, C. Yan, Y. Li, and Y. Su, "Chirp-free optical modulation using a silicon push–pull coupling microring," Opt. Lett. **34**, 785–787 (2009).

22. W. D. Sacher, W. M. J. Green, S. Assefa, T. Barwicz, H. Pan, S. M. Shank, Y. A. Vlasov, and J. K. S. Poon, "28 Gb/s silicon microring modulation beyond the linewidth limit by coupling modulation," in *Optical Fiber Communication Conference*, Technical Digest (CD) (Optical Society of America, 2012), paper OM3J.2.

23. Y. Li, L. Zhang, M. Song, B. Zhang, J. Yang, R. G. Beausoleil, A. E. Willner, and P. D. Dapkus, "Coupled-ring-resonator-based silicon modulator for enhanced performance," Opt. Express **16**, 13342–13348 (2008).

24. W. S. Fegadolli, G. Vargas, X. Wang, F. Valini, L. A. M. Barea, J. E. B. Oliveira, N. Frateschi, A. Scherer, V. R. Almeida, and R. R. Panepucci, "Reconfigurable silicon thermo-optical ring resonator switch based on Vernier effect control," Opt. Express **20**, 14722–14733 (2012).

25. P. Koonath, T. Indukuri, and B. Jalali, "3-D integrated Vernier filters in silicon," in *Integrated Photonics Research and Applications/Nanophotonics*, Technical Digest (Optical Society of America, 2006), paper IMG1.

26. B. Timotijevic, G. Mashanovich, A. Michaeli, O. Cohen, V. M. N. Passaro, J. Crnjanski, and G. T. Reed, "Tailoring the spectral response of add/drop single and multiple resonators in silicon-on-insulator," Chinese Opt. Lett. **7**, 291–295 (2009).

27. R. Boeck, N. A. F. Jaeger, N. Rouger, and L. Chrostowski, "Series-coupled silicon racetrack resonators and the Vernier effect: theory and measurement," Opt. Express **18**, 25151–25157 (2010).

28. J. Scheuer, G. T. Paloczi, and A. Yariv, "All optically tunable wavelength-selective reflector consisting of coupled polymeric microring resonators," Appl. Phys. Lett. **87**, 251102 (2005).

29. J. V. Hryniewicz, P. P. Absil, B. E. Little, R. A. Wilson, and P.-T. Ho, "Higher order filter response in coupled microring resonators," IEEE Photon. Technol. Lett. **12**, 320–322 (2000).

30. R. Grover, V. Van, T. A. Ibrahim, P. P. Absil, L. C. Calhoun, F. G. Johnson, J. V. Hryniewicz, and P.-T. Ho, "Parallel-cascaded semiconductor microring resonators for high-order and wide-FSR filters," J. Lightwave Technol. **20**, 900–905 (2002).

31. T. Wang, Z. Zhang, F. Liu, T. Ye, J. Wang, Y. Tian, M. Qiu, and Y. Su, "Modeling of quasi-grating sidewall corrugation in SOI microring add-drop filters," Opt. Commun. **282**, 3464–3467 (2009).

32. Q. Li, Z. Zhang, J. Wang, M. Qiu, and Y. Su, "Fast light in silicon ring resonator with resonance-splitting," Opt. Express **17**, 933–940 (2009).

33. T. Wang, F. Liu, J. Wang, Z. Zhang, T. Ye, Y. Tian, M. Qiu, and Y. Su, "Pulse delay and advancement in SOI microring resonators with mutual mode coupling," J. Lightwave Technol. **27**, 4734–4743 (2009).

34. Q. Li, Z. Zhang, F. Liu, M. Qiu, and Y. Su, "Dense wavelength conversion and multicasting in a resonance-split silicon microring," Appl. Phys. Lett. **93**, 081113 (2008).

35. Q. Chang, Q. Li, Z. Zhang, M. Qiu, and Y. Su, "Micrometer-scale optical up-converter using a resonance-split silicon microring resonator in radio over fiber systems," in *Optical Fiber Communication Conference*, Technical Digest (CD) (Optical Society of America, 2009), paper JWA48.

36. B. Little, J. Laine, and S. Chu, "Surface-roughness-induced contradirectional coupling in ring and disk resonators," Opt. Lett. **22**, 4–6 (1997).

37. S. Manipatruni, Q. Xu, B. Schmidt, J. Shakya, and M. Lipson, "High speed carrier injection 18 Gb/s silicon micro-ring electro-optic modulator," in *Proceedings of LEOS* (IEEE, 2007), pp. 537–538.

38. G. Li, X. Zheng, J. Yao, H. Thacker, I. Shubin, Y. Luo, K. Raj, J. E. Cunningham, and A. V. Krishnamoorthy, "25 Gb/s 1V-driving CMOS ring modulator with integrated thermal tuning," Opt. Express **19**, 20435–20443 (2011).

39. W. A. Zortman, A. L. Lentine, D. C. Trotter, and M. R. Watts, "Low-voltage differentially-signaled modulators," Opt. Express **19**, 26017–26026 (2011).

40. R. A. Soref and B. R. Bennett, "Kramers-Kronig analysis of E-O switching in silicon," Proc. SPIE **704**, 32–37 (1986).

41. S. Fathpour, K. K. Tsia, and B. Jalali, "Two-photon photovoltaic effect in silicon," J. Lightwave Technol. **3**, 1211–1217 (2007).

42. A. Yariv, "Coupled-mode theory for guided-wave optics," IEEE J. Quantum Eletron. **9**, 919–933 (1973).

43. T. Barwicz, M. A. Popović, F. Gan, M. S. Dahlem, C. W. Holzwarth, P. T. Rakich, E. P. Ippen, F. X. Kärtner, and H. I. Smith, "Reconfigurable silicon photonic circuits for telecommunication applications," Proc. SPIE **6872**, 68720Z, (2008).

44. M. A. Popović, T. Barwicz, F. Gan, M. S. Dahlem, C. W. Holzwarth, P. T. Rakich, H. I. Smith, E. P. Ippen, and F. X. Kärtner, "Transparent wavelength switching of resonant filters," presented at the Conference on Lasers and Electro-Optics, Baltimore, MD, USA May 2007.

45. P. Dong, W. Qian, H. Liang, R. Shafiiha, N. Feng, D. Feng, X. Zheng, A. V. Krishnamoorthy, and M. Asghari, "Low power and compact reconfigurable multiplexing devices based on silicon microring resonators," Opt. Express **18**, 9852–9858 (2010).

46. F. Shinobu, N. Ishikura, Y. Arita, T. Tamanuki, and T. Baba, "Continuously tunable slow-light device consisting of heater-controlled silicon microring array," Opt. Express **19**, 13557–13564 (2011).

47. N. M. Wright, D. J. Thomson, K. L. Litvinenko, W. R. Headley, A. J. Smith, A. P. Knights, J. H. B. Deane, F. Y. Gardes, G. Z. Mashanovich, R. Gwilliam, and G. T. Reed, "Free carrier lifetime modification in silicon," Proc. SPIE **7220**, 722006 (2009).

48. S. Xiao, M. H. Khan, H. Shen, and M. Qi, "Compact silicon microring resonators with ultra-low propagation loss in the C band," Opt. Express **15**, 14467–14475 (2007).

49. C. Manolatou and M. Lipson, "All-optical silicon modulators based on carrier injection by two-photon absorption," J. Lightwave Technol. **24**, 1433–1439 (2006).

50. M. R. Watts, D. C. Trotter, R. W. Young, and A. L. Lentine, "Ultralow power silicon microdisk modulators and switches," in *Proceedings of 5th IEEE International Conference on Group IV Photonics* (IEEE 2008), pp. 4–6.